crystals

MDPI

Article

Light-Programmable Ferroelectric Domain Walls in Thin-Film Lithium Niobate: A Multiphysics Simulation Study

Yunfei Niu [1,2,3,*], Luning Qian [4] and Chunchun Bei [5]

[1] Nanxun Innovation Institute, Zhejiang University of Water Resources and Electric Power, Hangzhou 310018, China
[2] School of Mechanical Engineering, Zhejiang University of Water Resources and Electric Power, Hangzhou 310018, China
[3] National Laboratory of Solid State Microstructures, Nanjing University, Nanjing 210093, China
[4] School of Intelligent Construction, Zhejiang Construction Technician College, Hangzhou 310018, China
[5] Zhejiang Hangzhou Ecological Environment Monitoring Center, Hangzhou 310007, China
* Correspondence: niuyf@zuwe.edu.cn

Abstract

Conductive ferroelectric domain walls in lithium niobate combine nonvolatile, multilevel memristive conductance with the strong electro-optic response of the host crystal, which makes them attractive functional elements for reconfigurable photonic devices on the thin-film lithium niobate platform. Here we report a multiphysics simulation study of how the domain-wall conductance, and therefore the electro-optically transduced optical response, can be programmed by illumination and temperature. The screening-charge relaxation is modelled as a thermally activated dark process combined with a photo-induced contribution from above-band-gap illumination; the predicted relaxation time decreases with both increasing temperature and increasing illumination. We examine three alternative photoconductivity models and find that the qualitative behaviour—the existence of an optimum illumination window and the direction of the tuning trends—is independent of the assumed functional form, while the quantitative relaxation time depends on it. Within the model, three device-level capabilities are predicted: light-tuned fading memory with an optimum illumination window in which the one-step prediction error of a chaotic time series improves by a factor of 1.7; optical assistance that enables low-voltage multilevel nonvolatile programming; and thermal robustness of the memory capacity over an extended temperature range of 250–400 K. A parameter-sensitivity analysis shows that the memory capacity remains within 0.98–1.02 for all parameter variations examined, whereas the one-step prediction error varies by less than a factor of 1.6. We additionally quantify the system-level energy budget including illumination and thermal control, estimate the interferometer operating limits, and present the light-absorption and domain-switching considerations that define the experimental conditions. All results are model predictions and are intended to guide and be tested by experiments; experimental verification in a thin-film lithium niobate interferometer remains to be performed.

Keywords: thin-film lithium niobate; ferroelectric domain wall; domain engineering; photoconductivity; screening dynamics; electro-optic effect; memristive device; reconfigurable photonics

Check for updates

Academic Editor: Ram S. Katiyar

Received: 4 September 2026
Revised: 21 September 2026
Accepted: 27 September 2026
Published: 30 September 2026

Copyright: © 2026 by the authors. Licensee MDPI, Basel, Switzerland. This article is an open access article distributed under the terms and conditions of the Creative Commons Attribution (CC BY) license.

1. Introduction

Reconfigurable integrated photonics underpins programmable optical circuits, photonic neural networks and adaptive signal processing. Thin-film lithium niobate (TFLN) has become a leading platform for such circuits because it combines the large Pockels coefficient of $LiNbO_3$ crystals ($r_{33} \approx 31$ pm/V) with wafer-scale fabrication and CMOS-compatible drive voltages [1–3]. Electro-optically programmable linear circuits [4] and programmable optical filters [5] have been demonstrated, and ferroelectric domain engineering in lithium niobate films has matured into a precise tool for tailoring light–matter interaction at the micro- and nanoscale [6].

Charged ferroelectric domain walls (DWs)—the nanoscale interfaces separating oppositely poled domains—are conductive and memristive: their conductance is set by the distribution of screening charge [7,8], and DW-based devices have exhibited nonvolatile memory [9,10] and analog synaptic behaviour [11]. The conductance of a DW is not a fixed crystal property. It can be modified by defect engineering and reduction [12,13], tuned by mechanical stress through the piezoelectric effect [14], adjusted by the DW inclination and by the poling conditions [7,8], and modified by temperature, with activation energies ranging from ≈0.1 eV for stable low-temperature DW currents [15] to 0.8–1.1 eV at high temperature or in doped and reduced crystals [15,16]. Light also affects DW transport: photo-induced electronic transport along charged walls has been measured [17], and optically programmable TFLN devices—including an optically programmable, erasable and rewritable photonic molecule in a single racetrack resonator [18]—have recently been demonstrated. Ultrafast delay-line photonic reservoir computing has likewise advanced on this platform [19,20].

These results suggest that a DW inside a TFLN waveguide could act as a light-programmable functional element, in which the same physical wall provides memory, nonlinearity and electro-optic readout. However, before such a device can be designed, two questions must be answered quantitatively: how do illumination and temperature set the DW conductance dynamics, and what device-level performance follows from them? Neither question has been addressed in a unified model. The present work is a simulation study that addresses both questions and, equally importantly, identifies what has to be measured to validate the picture.

We model the DW screening-charge relaxation with an RC-type time constant that depends on the sum of a thermally activated dark conductivity and a photo-induced conductivity, and we embed this relation in a dual-timescale (volatile plus nonvolatile) conductance model coupled to the Pockels response of a TFLN Mach–Zehnder interferometer (MZI). We then examine, in simulation: (i) the numerical consistency of the relaxation law; (ii) the sensitivity of the predictions to the assumed photoconductivity model; (iii) the illumination dependence of the memory capacity and of four computing tasks; (iv) the temperature dependence over an extended range (250–400 K); (v) the sensitivity to the full parameter set; (vi) the system-level energy budget including illumination and thermal control; and (vii) the interferometer operating limits and the retention of the nonvolatile state. We also specify the illumination conditions (wavelength, continuous-wave versus pulsed operation, focusing, polarization) and the light-absorption and domain-switching considerations that determine whether the predicted effects can be observed. Throughout, we distinguish clearly between model predictions, which are the results of this work, and experimental demonstrations, which do not yet exist for the proposed configuration.

2. Materials and Methods

2.1. Device Structure, Illumination Configuration and Readout

The simulated device (Figure 1a) is an x-cut congruent TFLN rib waveguide (film thickness 600 nm, etch depth 350 nm, rib width 1.2 μm) forming one arm of an MZI with interaction length L = 5 mm at λ = 1550 nm. A ferroelectric DW is written beneath a coplanar comb-electrode pair (gap d = 4 μm) by room-temperature electric-field poling, following the DW-writing approaches used for TFLN [8]. Two external channels act on this wall:

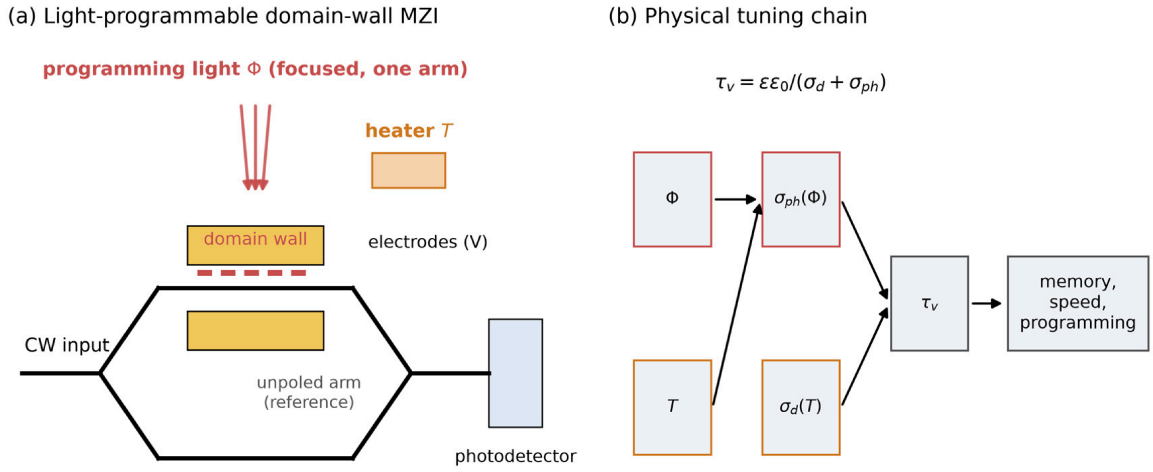


Figure 1. (**a**) Layout of the simulated light-programmable domain-wall Mach–Zehnder device: a continuous-wave input is split between two arms; a ferroelectric domain wall is written under the comb electrodes of one arm; a focused programming beam (continuous-wave or pulsed, polarized along the extraordinary axis) illuminates that arm; an integrated heater sets the temperature; and the output is detected. (**b**) Physical tuning chain: illumination and temperature set the photo-induced and dark conductivities, whose sum sets the screening time and hence the memory, speed and programming behaviour.

Optical channel. A programming beam illuminates the electrode region of one arm, focused to a spot comparable to or smaller than the electrode gap (Figure 1a). Two regimes are considered in the analysis: continuous-wave (CW) illumination, which establishes a steady photocarrier density and hence a steady photo-induced conductivity; and pulsed illumination (nanosecond to microsecond pulses), which additionally allows the writing/erasure energy to be defined (Sections 3.8 and 4.1). We take the illumination to be above the electronic absorption edge of the material—either intrinsic ($\lambda \lesssim 310$ nm for the ≈4.0 eV band gap of $LiNbO_3$) or, more practically for on-chip integration and for avoiding strong two-photon effects, sub-band-gap visible light (405–532 nm) that generates carriers through defect and impurity states (photorefractive/defect-mediated absorption) [6,21]. The beam is polarized along the extraordinary axis to couple to the largest electro-optic coefficient (r_{33}) and, where relevant, to the DW conductivity; the influence of polarization is discussed in Section 4.1. The optical intensity is expressed in normalized units, $\Phi = I/I_{sat}$, with I_{sat} the intensity at which the photo-induced conductivity saturates; for the energy estimates of Section 3.8, $I_{sat} = 1$ W cm^{-2} is assumed, which is representative of photorefractive and photoconductive responses in $LiNbO_3$ [6,21].

Thermal channel. An integrated heater sets the device temperature T; the analysis covers 250–400 K, which spans the range relevant to packaged photonic circuits.

Readout. The MZI output intensity is read by a photodetector on the output waveguide (Figure 1a). The output is $I_{out}/I_{in} = \cos^2[(\pi/2 + \Delta\varphi)/2]$, where the Pockels phase shift is $\Delta\varphi = (2\pi/\lambda)\cdot(-\frac{1}{2}\, n_e^3\, r_{33}\, \Gamma\, V_{DW}/d)\cdot L$, with $n_e = 2.138$, $\Gamma = 0.80$ (computed with a scalar

finite-difference Helmholtz eigenmode solver; n_{eff} = 1.900) and V_{DW} the voltage dropped across the DW branch (Section 2.4).

2.2. Screening-Charge Relaxation

The DW conductance relaxes because the screening charge redistributes through a conductive medium of total conductivity σ_{tot}. The relaxation is RC-type with time constant

$$\tau_v(\Phi, T) = \frac{\varepsilon\varepsilon_0}{\sigma_d(T) + \sigma_{ph}(\Phi)} \quad (1)$$

where ε = 30 is the effective dielectric constant of the LN film stack and ε_0 the vacuum permittivity. The dark conductivity is thermally activated,

$$\sigma_d(T) = \sigma_{d0} \exp\left[\frac{E_a}{k_B}\left(\frac{1}{T_0} - \frac{1}{T}\right)\right] \quad (2)$$

with reference temperature T_0 = 300 K and activation energy E_a. We use E_a = 0.1 eV as the reference value, consistent with the ≈0.1 eV activation reported for stable low-temperature DW currents in $LiNbO_3$ [15]; because the Arrhenius factor in Equation (2) equals unity at $T = T_0$ by construction, E_a influences the results only away from 300 K, and its sensitivity is therefore examined at 350 K (Section 3.7). Reported values for DW and reduced-crystal transport span 0.1–1.1 eV [15,16], and this range is used in the sensitivity analysis.

2.3. Photoconductivity Models

The photo-induced conductivity is not known a priori for a given TFLN/DW system, and its functional form depends on the dominant recombination path. We therefore examine three representative forms rather than assuming a single one:

$$\text{saturating (recombination/trap limited)}: \ \sigma_{ph}(\Phi) = \sigma_{ph}^{max}\,\Phi/(\Phi + \Phi_{sat}) \quad (3a)$$

$$\text{linear (monomolecular, low injection)}: \ \sigma_{ph}(\Phi) = \sigma_{ph}^{max}\,\Phi/\Phi_{sat} \quad (3b)$$

$$\text{sub-linear (bimolecular, high injection)}: \ \sigma_{ph}(\Phi) = \sigma_{ph}^{max}\sqrt{\Phi/\Phi_{sat}} \quad (3c)$$

Throughout, the photo-induced conductivity is normalized so that $\sigma_{ph} = \sigma_{ph}^{max}$ at $\Phi = \Phi_{sat}$, with $\sigma_{ph}^{max} = 4\sigma_{d0}$ (T_0) in the reference case; the ratio $\sigma_{ph}^{max}/\sigma_{d0}$ is varied in Section 3.7. Equation (3a–c) bracket the physically plausible behaviour: linear in the low-injection limit, square-root in the bimolecular high-injection limit, and saturating when trap filling or recombination limits further carrier generation. Section 3.2 quantifies how the choice affects the predictions.

2.4. Dual-Timescale Conductance Dynamics

The DW conductance is decomposed as $G(t) = G_0 + G_v(t) + G_{nv}(t)$, with baseline G_0 = 1 μS; G_v is the volatile component whose nanosecond relaxation provides short-term (fading) memory, and G_{nv} is the nonvolatile component that stores the programmed weight:

$$\frac{dG_v}{dt} = \alpha_v |I_{tot}| \sinh\left(\frac{V}{V_0}\right)\left(1 - \frac{G_v}{G_v^{max}}\right) - \frac{G_v}{\tau_v(\Phi, T)} \quad (4)$$

$$\frac{dG_{nv}}{dt} = \alpha_{nv}(\Phi) |I_{tot}| \sinh\left(\frac{V}{V_0}\right)\left(1 - \frac{G_{nv}}{G_{nv}^{max}}\right) - \frac{G_{nv}}{\tau_{nv}} \quad (5)$$

with V_0 = 0.6 V, G_v^{max} = 0.65 μS, G_{nv}^{max} = 1.9 μS, τ_{nv} = 4.2 s and $\alpha_v = 2.4 \times 10^7\ S^{-1}$. Illumination enters in three places: through $\tau_v(\Phi,T)$ in Equation (1); through a photo-enhanced screening drive, $I_{tot} = V \cdot G \cdot (1 + \eta_{ph}\,\Phi)$ with η_{ph} = 2, which represents the addi-

tional photocarrier-assisted screening current; and through a photo-accelerated write rate, $\alpha_{nv}(\Phi) = \alpha_{nv0} \cdot [1 + 3\Phi/(\Phi + \Phi_{sat})]$ with $\alpha_{nv0} = 3.0 \times 10^4\ S^{-1}$. The physical roles of these terms are as follows: α_v and α_{nv} set how efficiently the applied field redistributes the screening charge in the volatile and nonvolatile channels, respectively; η_{ph} parameterizes the additional photocarrier contribution to the screening current; $G_v{}^{max}$ and $G_{nv}{}^{max}$ bound the two conductance ranges through the phenomenological saturation factors $(1 - G/G^{max})$; and τ_{nv} sets the dark retention. The saturation form of G_v and G_{nv} follows the standard drift-type memristor description used for $LiNbO_3$ DW devices [7,8], in which the conductance approaches a maximum as the available screening charge is exhausted. The sensitivity of the predictions to all of these parameters is quantified in Section 3.7. Table 1 lists the reference values of all parameters together with the ranges examined.

Table 1. Model parameters (reference case, comb-electrode geometry).

Parameter	Symbol	Reference Value	Range Examined
Effective dielectric constant	ε	30	20–40
Dark-conductivity prefactor (300 K)	σ_d0	4.58×10^{-2} S/m	×0.5–×2
Activation energy	E_a	0.10 eV	0.05–0.30 eV
Max. photo-induced conductivity	σ_phˆmax	4σ_d0	×2–×8
Photo-drive coefficient	η_ph	2	0–4
Volatile relaxation (dark, 300 K)	τ_v	5.80 ns	—
Nonvolatile relaxation	τ_nv	4.2 s	4.2–10^5 s
Saturation intensity	I_sat	1 W cm^{-2}	assumed
Symbol period/virtual nodes	T, N	8 ns, 20	—

2.5. Electro-Optic Readout and Interferometer Operating Limits

The conductance sets the voltage dropped across the DW branch, $V_{DW} = V \cdot G_{ser}/(G_{ser} + G)$ with series conductance $G_{ser} = 2.5$ μS, which produces the Pockels phase shift defined in Section 2.1. Three operating limits are evaluated: (i) the small-signal bandwidth, $f_{3dB} = 1/(2\pi\tau_v)$, set by the screening relaxation; (ii) the modulation window and the dynamic range, obtained by evaluating the transfer function of Section 2.1 over the bias range at several illumination levels; because the transfer function does not reach zero, the dynamic range is quoted for a 10^{-4} detection floor; and (iii) the shot-noise-limited detection signal-to-noise ratio versus received optical power.

2.6. Sensitivity Analysis Method

The sensitivity of the predicted device behaviour—the relaxation time at $\Phi = 0.3$, the memory capacity, and the one-step Mackey–Glass prediction error—is evaluated by varying one parameter at a time, keeping the others at their reference values: the effective dielectric constant (ε = 20, 40), the dark-conductivity prefactor ($\sigma_{d0} \times 0.5, \times 2$), the maximum photo-induced conductivity ($\sigma_{ph}{}^{max} \times 2, \times 8$), the photo-drive coefficient (η_{ph} = 0, 4), and the activation energy (E_a = 0.05, 0.10, 0.20, 0.30 eV, evaluated at 350 K as explained in Section 2.2).

2.7. Benchmarks and Metrics

Because a single benchmark cannot establish a general computational advantage, four tasks are evaluated as a function of illumination: (i) one-step Mackey–Glass prediction (τ = 17), reported as normalized mean-square error (NMSE) [22]; (ii) NARMA-2 system identification [23]; (iii) four-level nonlinear channel equalization at 28 dB signal-to-noise ratio [20], reported as symbol error rate (SER); and (iv) sine/square waveform classification, reported as accuracy. In each case the reservoir state is the vector of MZI output intensities sampled at 20 virtual nodes per input symbol (node spacing 0.4 ns, symbol period 8 ns),

read out by closed-form ridge regression (regularization 10−6–10−5). The linear short-term memory capacity is reported as MC = Σ_k corr2(y_k, u(t − k)), k = 1…10. All simulations use fixed random seeds and are reproducible with the provided code (Supplementary Materials). The Mackey-Glass benchmark follows the original formulation of Mackey and Glass [24].

3. Results

3.1. Screening-Time Law and Its Numerical Consistency

Figure 2a shows the relaxation time of Equation (1) versus illumination for T = 270, 300 and 330 K, together with relaxation times extracted from the simulated decay of the volatile conductance after a 2 ns drive pulse. The extracted values agree with Equation (1) to within 0.1 ns at dark and moderate illumination (5.79 vs. 5.80 ns at Φ = 0; 3.01 vs. 3.02 ns at Φ = 0.3; 1.97 vs. 1.93 ns at Φ = 1.0). At strong illumination (Φ = 3) the extracted value (1.88 ns) exceeds the model value (1.45 ns), because the photo-enhanced drive saturates the volatile state; this deviation is itself a model prediction that marks the onset of the saturation regime analysed in Section 3.3. We emphasize that this is an internal consistency check between the relaxation law and the time-domain integration of the same model; it is not a validation against experimental data, which does not yet exist for this configuration (Section 4.2).

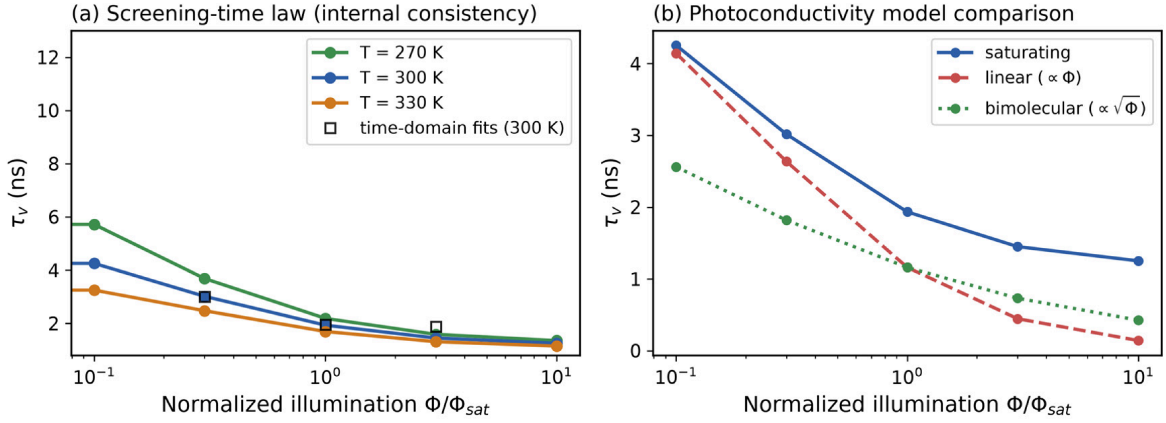


Figure 2. (**a**) Screening-time law of Equation (1) versus normalized illumination at 270, 300 and 330 K, together with relaxation times extracted from the simulated time-domain response at 300 K (open squares). (**b**) Sensitivity of the predicted relaxation time to the photoconductivity model: saturating (Equation (3a)), linear (Equation (3b)) and sub-linear/bimolecular (Equation (3c)).

3.2. Sensitivity to the Photoconductivity Model

Figure 2b compares the relaxation time predicted by the three photoconductivity models of Equations (3) at 300 K. All three reproduce the central qualitative feature—a monotonic decrease in τ_v with illumination—but they differ quantitatively at strong illumination: at Φ = 3, τ_v = 1.45, 0.45 and 0.73 ns for the saturating, linear and sub-linear models, respectively. The device-level consequences are remarkably similar (Table 2): at the optimum illumination (Φ = 0.3) the one-step Mackey–Glass NMSE is 3.30 × 10^{-3}, 3.22 × 10^{-3} and 3.09 × 10^{-3} for the three models, respectively, and the degradation at strong illumination occurs at the same illumination level in all cases. The existence of an optimum illumination window, and the direction of all tuning trends, are therefore independent of the assumed functional form; only the numerical value of τ_v at high illumination depends on it. This is important for the experimental outlook, because the qualitative design rules can be tested without knowing the photoconductivity law in advance, while a quantitative match will require measuring it (Section 4.2).

Table 2. Predicted performance versus illumination for the four benchmark tasks (comb geometry, 300 K). MC: memory capacity (symbols); MG: one-step Mackey–Glass NMSE; SER: channel-equalization symbol error rate.

Φ/Φ_sat	MC	MG NMSE	NARMA-2 NMSE	SER	Sine/Square Acc.
0 (dark)	0.96	5.75×10^{-3}	0.565	0.051	86.2%
0.1	1.00	3.98×10^{-3}	0.493	0.047	86.2%
0.3	1.01	3.30×10^{-3}	0.435	0.049	86.0%
1.0	1.01	6.16×10^{-3}	0.400	0.055	86.7%
3.0	0.72	1.14×10^{-2}	0.572	0.060	87.0%
10.0	0.13	2.11×10^{-2}	0.967	0.073	89.7%

3.3. Light-Tuned Fading Memory

The memory capacity versus illumination is reported in Table 2. Moderate illumination improves memory coupling: MC rises from 0.96 (dark) to 1.00–1.01 at Φ = 0.1–1.0. Beyond $\Phi \approx 1$ the wall saturates: the photo-enhanced drive pins G_v near its maximum, the state loses sensitivity to the input, and MC falls to 0.72 (Φ = 3) and 0.13 (Φ = 10). The response is therefore non-monotonic, with an optimum window $\Phi \approx$ 0.1–1.0 Φ_{sat}. The corresponding task-level behaviour is shown in Figure 4b.

3.4. Predicted Multilevel Optical Programming

Figure 3b shows the predicted effect of optical assistance on nonvolatile programming. With 0.5 V programming pulses and no illumination, the programmed state changes negligibly over 60 pulses (no resolvable levels at 0.5% read-intensity resolution). With optical assistance ($\Phi = 5\ \Phi_{sat}$) the same pulse train produces a monotonic staircase corresponding to 12 resolvable read-intensity levels. These are predicted performance figures obtained from the model, not measured device performance; they define a target for experiments (Section 4.2). The static current–voltage window is preserved under illumination (Figure 3a; on/off ratio 7.2 in both cases), i.e., the optical channel modifies the write dynamics without degrading the static memristive window in the model.

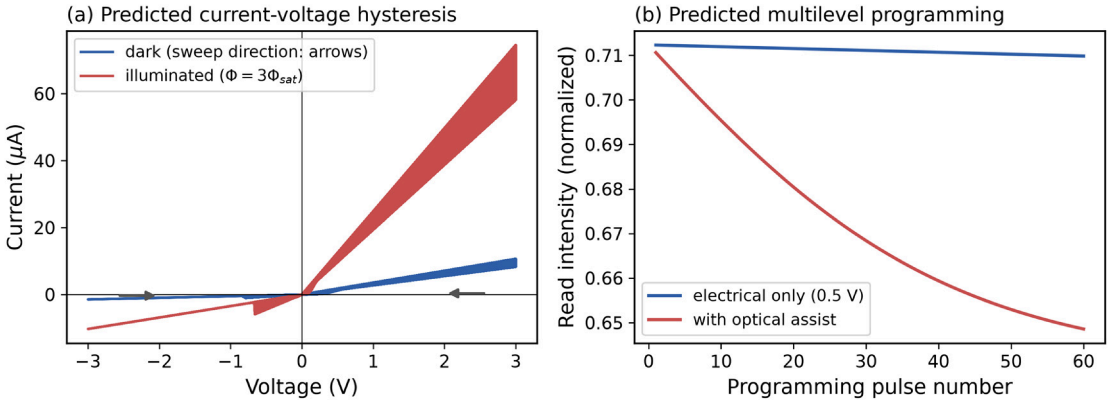


Figure 3. (**a**) Predicted current-voltage characteristic of the domain-wall branch in the dark and under illumination ($\Phi = 3\Phi_{sat}$); the arrows indicate the direction of the voltage sweep, and the memristive window is preserved under illumination (on/off ratio 7.2). (**b**) Predicted nonvolatile programming under 60 low-bias (0.5 V) pulses without illumination and with optical assistance; the optical assist produces a staircase of 12 resolvable read-intensity levels.

3.5. Thermal Behaviour over an Extended Range

The reviewers noted that the original analysis was restricted to 270–330 K. Figure 4a extends the range to 250–400 K. The relaxation time decreases from 12.6 ns at 250 K to 2.2 ns at 400 K, following Equation (2), while the memory capacity remains in the narrow

range 0.95–0.99 across the entire window. The one-step prediction error improves modestly with increasing temperature (7.4×10^{-3} at 250 K to 4.1×10^{-3} at 400 K), because the shortening of τ_v brings the system closer to the operating point analysed in Section 3.3. We therefore restrict our claims to the simulated range 250–400 K and note explicitly that behaviour outside this window—in particular near the ferroelectric phase transition, where the material parameters and the domain structure change—is not covered by the model.

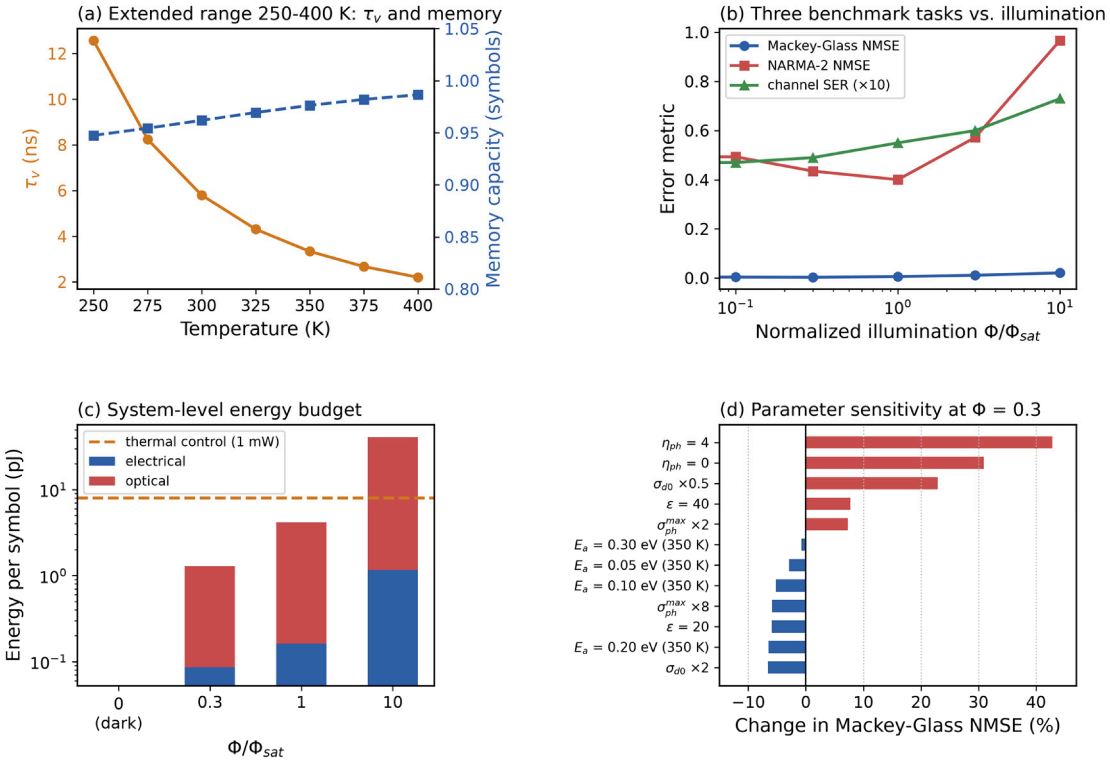


Figure 4. (**a**) Extended temperature range (250–400 K): the relaxation time decreases with temperature while the memory capacity remains within 0.95–0.99. (**b**) Four benchmark tasks versus illumination, showing the task-dependent optimum. (**c**) System-level energy budget per symbol, including electrical, optical and thermal contributions. (**d**) Parameter sensitivity of the one-step prediction error at $\Phi = 0.3$. In (**d**) the bars show the relative change in the one-step Mackey-Glass prediction error caused by each parameter variation; positive (red) and negative (blue) bars indicate an increase and a decrease of the error, respectively.

3.6. Multi-Task Evaluation

Figure 4b and Table 2 report four benchmark tasks versus illumination. The optimum illumination is task-dependent: the chaotic-prediction error is minimized at $\Phi \approx 0.3$ (NMSE 3.30×10^{-3}), the NARMA-2 error is minimized at $\Phi \approx 1$ (0.400), the channel-equalization error is minimized at $\Phi \approx 0.1$ (SER 0.047), and the memory-light sine/square accuracy is nearly illumination-independent (86–90%). The underlying reason is that illumination trades memory depth against nonlinear drive strength: longer relaxation favours tasks requiring memory, while stronger photo-induced drive favours instantaneous nonlinearity. Rather than establishing a single "best" operating point, the model therefore predicts that illumination provides a tunable memory–nonlinearity balance that can be matched to the task, with the optimum window $\Phi \approx 0.1$–$1\ \Phi_{sat}$ common to all memory-dependent tasks.

3.7. Parameter Sensitivity

Figure 4d and Table 3 summarize the sensitivity analysis. The relaxation time is most sensitive to the dark-conductivity prefactor and to the effective dielectric constant, as expected from Equation (1): $\sigma_{d0} \times 0.5$ increases τ_v to 6.03 ns and $\sigma_{d0} \times 2$ decreases it

to 1.51 ns, while ε = 20 and 40 give 2.01 and 4.02 ns, respectively. The maximum photo-induced conductivity and the photo-drive coefficient have a weaker influence on τ_v but a clear influence on the optimum: removing the photo-drive term (η_{ph} = 0) degrades the best prediction error from 3.30×10^{-3} to 4.33×10^{-3}, confirming that the improvement in Section 3.3 is not an artefact of a single parameter choice. The activation energy matters only away from 300 K, as expected: at 350 K, τ_v varies from 2.59 ns (E_a = 0.05 eV) to 0.94 ns (E_a = 0.30 eV). Crucially, the memory capacity remains within 0.98–1.02 for every variation examined, and the prediction error varies by less than a factor of 1.6 (3.09×10^{-3} to 4.72×10^{-3}). The predicted device-level capabilities are therefore robust to the parameter uncertainties identified by the reviewers, although the quantitative optimum illumination shifts with ${\sigma_{ph}}^{max}$.

Table 3. Parameter sensitivity at Φ = 0.3 (T = 300 K unless stated). Values are the relaxation time τ_v, the one-step Mackey–Glass NMSE, and the memory capacity.

Variation	τ_v (ns)	MG NMSE	MC
Reference	3.02	3.30×10^{-3}	1.01
ε = 20	2.01	3.11×10^{-3}	1.01
ε = 40	4.02	3.56×10^{-3}	1.01
σ_d0 × 0.5	6.03	4.06×10^{-3}	1.01
σ_d0 × 2	1.51	3.09×10^{-3}	1.01
σ_phˆmax × 2	3.97	3.55×10^{-3}	1.01
σ_phˆmax × 8	2.04	3.11×10^{-3}	1.01
η_ph = 0	3.02	4.33×10^{-3}	0.98
η_ph = 4	3.02	4.72×10^{-3}	1.02
E_a = 0.05 eV (350 K)	2.59	3.21×10^{-3}	1.01
E_a = 0.10 eV (350 K)	2.18	3.13×10^{-3}	1.01
E_a = 0.20 eV (350 K)	1.47	3.09×10^{-3}	1.01
E_a = 0.30 eV (350 K)	0.94	3.28×10^{-3}	1.00

3.8. System-Level Energy Budget

The reviewers correctly noted that the electrical drive energy alone does not represent the complete energy budget. Figure 4c and Table 4 report the system-level budget, including the optical energy required to establish the illumination and the thermal energy required for temperature control. Using I_{sat} = 1 W cm^{-2} over an illuminated area of 10 µm × 5 mm, the optical power is 150 µW at Φ = 0.3 and 5 mW at Φ = 10, corresponding to 1.20 and 40.0 pJ per 8 ns symbol; the electrical drive energy is 0.05–1.16 pJ per symbol over the same range; and thermal control consumes ≈8 pJ per symbol for a representative 1 mW heater. The total energy per symbol at the optimum illumination window is therefore ≈1.3 pJ (electrical + optical) or ≈9.3 pJ when thermal control is included—one to two orders of magnitude above the electrical-only figure, but still in the picojoule range. We also note that the optical energy scales with the illuminated area, so that tighter focusing (or a resonant geometry) directly reduces the optical contribution; this is a design lever rather than a fundamental limit. Erase operation requires reversing the write bias (or removing the optical assistance); because the programming is symmetric in bias polarity in Equations (4) and (5), the erasure energy is of the same order as the write energy—0.09 pJ electrically at the optimum window, plus the same optical energy (1.20 pJ) if optical assistance is used.

Table 4. System-level energy budget per 8 ns symbol (assumptions as in Section 3.8).

Φ/Φ_sat	Optical Power	Electrical Energy	Optical Energy	Total (el. + opt.)	With 1 mW Thermal Control
0	0	0.05 pJ	0	0.05 pJ	8.05 pJ
0.3	150 µW	0.09 pJ	1.20 pJ	1.29 pJ	9.29 pJ
1.0	500 µW	0.16 pJ	4.00 pJ	4.16 pJ	12.2 pJ
10.0	5 mW	1.16 pJ	40.0 pJ	41.2 pJ	49.2 pJ

Erase: reversing the write bias requires the same energy as writing (0.09 pJ electrically at the optimum window, plus 1.20 pJ optically if assistance is used).

3.9. Operating Limits and Dark Retention

Figure 5 summarizes the interferometer operating limits. (a) The small-signal bandwidth set by the screening relaxation rises with illumination, from 27.4 MHz in the dark to 127 MHz at Φ = 10, so that light tunes not only the memory but also the modulation speed. (b) The transfer curves evaluated at three illumination levels show that the usable modulation window is preserved as the wall is illuminated. (c) The shot-noise-limited detection signal-to-noise ratio is plotted against received optical power for the dark and illuminated bandwidths, with a 20 dB detection threshold indicated; at 1 µW the SNR is ≈34.5 dB. Evaluated with the 10^{-4} detection floor defined in Section 2.5, the modulation dynamic range is ≈80 dB and is essentially illumination-independent, because the transfer function is set by the electro-optic response rather than by the DW dynamics. Finally, the retention of the nonvolatile state follows exp $(-t/\tau_{nv})$: with the conservative value τ_{nv} = 4.2 s used throughout (10% decay in 0.44 s), the state would relax too quickly for long-term storage, whereas values representative of pinned/stabilized walls (τ_{nv} = 10^3–10^5 s, see Section 4.1) give 10% decay times of 1.7 min to 2.9 h. Reported DW memory retention in $LiNbO_3$ depends strongly on wall pinning, screening stabilization and device design [9,10]; the retention time is therefore an experimental input that must be measured for a given fabrication process, and our model treats it as a parameter rather than a prediction.

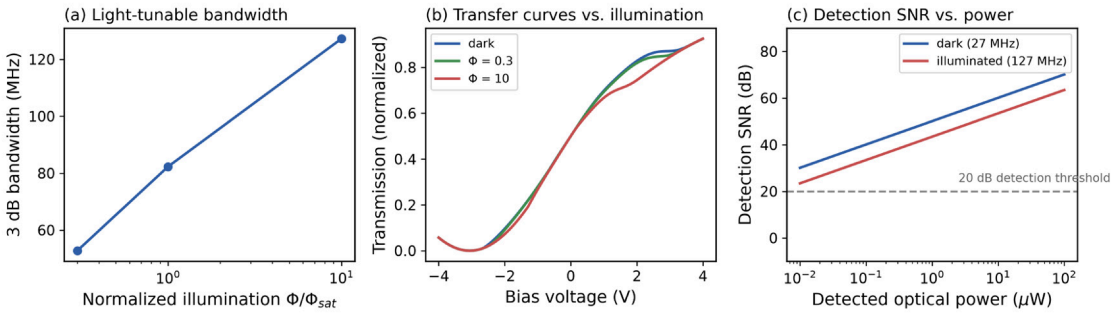


Figure 5. Predicted interferometer operating limits versus illumination: (**a**) small-signal bandwidth set by the screening relaxation, which increases with illumination; (**b**) transfer curves at three illumination levels (dark, Φ = 0.3 and Φ = 10); and (**c**) shot-noise-limited detection signal-to-noise ratio versus received optical power for the dark and illuminated bandwidths, with the 20 dB detection threshold indicated.

4. Discussion

4.1. Physical Mechanisms and Illumination Conditions

Several light-induced mechanisms coexist in $LiNbO_3$ and must be distinguished for the proposed device [6,15,17,21]. (i) Photoconductivity: above-band-gap or defect-mediated absorption creates electron–hole pairs that increase the conductivity, screening the depolarization field and thereby shortening τ_v—this is the mechanism modelled in Equations (1) and (3). (ii) Photorefractive effect: photo-excited carriers drift and are

retrapped, producing space-charge fields that modulate the refractive index; this is a competing effect that also modifies the interferometer response and must be separated experimentally (e.g., by comparing the DW branch with a reference branch without a wall). (iii) Pyroelectric effect and absorption-induced heating: absorption also heats the crystal, and the pyroelectric field can modify screening. The magnitude of this contribution can be estimated directly: for a weakly absorbing crystal (absorption coefficient $\alpha \approx 0.1$–$1\ \mathrm{cm}^{-1}$ at visible wavelengths), an intensity of $1\ \mathrm{W\ cm}^{-2}$ and a film thickness $t = 600$ nm, the absorbed power density is $\alpha I \leq 10^{6}\ \mathrm{W\ m}^{-3}$, which for a thermal conductivity $\kappa \approx 4\ \mathrm{W\ m}^{-1}\ \mathrm{K}^{-1}$ gives a steady-state temperature rise $\Delta T \approx \alpha I\, t^{2}/(2\kappa) \lesssim 10^{-6}$ K; even at ten times this intensity, ΔT remains below 10^{-5} K. Light-induced heating is therefore negligible in the intensity range considered, so the thermal channel of the model is dominated by the external heater and the light-induced effect is photoconductive/photorefractive rather than thermal. Conversely, high-intensity operation ($\gg 10^{3}\ \mathrm{W\ cm}^{-2}$) or strongly absorbing (e.g., reduced) crystals would bring the absorption contribution into play, and the transient pyroelectric response—not resolved here—would then need to be included. (iv) Domain switching: switching requires the local field to exceed the coercive field ($\approx$21 kV/mm in congruent $LiNbO_3$); with the drive voltages considered here ($\leq$3 V across a 4 µm gap, i.e., $\leq$0.75 kV/mm) and with the wall pre-written, illumination at moderate intensity is not expected to induce switching, but intense focused light can generate local fields that do; the switching threshold should therefore be measured before high-intensity operation. (v) Polarization dependence: because both the electro-optic response (r_{33}) and the photo-induced transport are anisotropic, the illumination should be polarized along the extraordinary axis for maximum effect; a systematic polarization study is part of the experimental protocol below.

The dark memory time (Section 3.9) belongs to the same discussion: DW retention is governed by the stability of the screening charge and by wall pinning, and reported values vary widely [9,10]. Our model treats τ_{nv} as an adjustable input and shows how retention scales with it, rather than claiming a specific retention.

4.2. Comparison with Experiment and Testable Predictions

We emphasize that all results in this work are model predictions. No experimental data for a DW-embedded TFLN MZI under controlled illumination and temperature exist yet, and the parameters of Equations (1)–(5) are taken from the published ranges for $LiNbO_3$ DW transport [7,8,12–17] rather than measured on a specific device. To make the study useful for experiment, we list the measurements that would test it:

1. Screening kinetics. Transient current or capacitance measurements on a poled TFLN MZI under stepped illumination, from which $\tau_v(\Phi)$ can be extracted and compared with Figure 2a. The predicted functional form (monotonic decrease, saturation onset near $\Phi \approx 1$) is model-independent (Section 3.2), so a qualitative test is feasible immediately. 2. Photoconductivity law. Steady-state photocurrent versus intensity, fitted to the forms of Equation (3a–c), which would fix the quantitative branch of Figure 2b. 3. Temperature dependence. τ_v (T) between 250 and 400 K, which gives the activation energy E_a directly and tests Section 3.5. 4. Programming. Pulsed write at low bias ($\pm$0.5 V) with and without optical assistance, comparing the number of resolvable read levels with the predicted 12 (Section 3.4). 5. Retention. Dark decay of a programmed state over hours to days, which fixes τ_{nv} (Section 3.9). 6. Mechanism separation. Comparative measurements on a reference MZI without a DW, and polarization-resolved measurements, to separate photoconductivity from photorefraction and pyroelectric contributions (Section 4.1).

Recommended measurement configuration: a Mach–Zehnder interferometer of the layout in Figure 1a, with the DW written in one arm, a free-space or fibre-coupled pro-

gramming beam focused onto the electrode region, a resistive heater and thermometer for temperature control, and balanced detection at the output. The comb-electrode geometry of Figure 1a is convenient because it concentrates the field close to the wall (as in our previous electrostatic analysis of electrode geometries), but the framework of Equations (1)–(5) is independent of the electrode geometry.

4.3. Limitations

The following limitations should be stated explicitly. (i) The model is two-dimensional and uses an idealized device geometry; three-dimensional field distributions in the actual poled structure, and the fabrication-related variations in both the wall and the electrodes, are not captured. A full three-dimensional electrostatic/transport model, and eventually metrology on fabricated devices, would be required for quantitative device design. (ii) The parameters are literature-calibrated, not measured; Section 3.7 shows which of them matter most (σ_{d0}, ε) and which are least constrained (the photoconductivity law, τ_{nv}). (iii) The optical model is scalar and lossless: insertion loss, residual amplitude modulation and the thermal drift of the MZI bias point are not included, and the propagation of the programming beam inside the waveguide is treated only through the absorbed intensity. (iv) The energy budget uses representative assumptions for the illuminated area and the thermal load, which should be replaced by measured values. (v) The thermal analysis is limited to 250–400 K by construction and does not include the ferroelectric phase transition or high-temperature ionic conduction. (vi) Finally, the whole framework awaits experimental verification in the TFLN MZI configuration proposed here.

5. Conclusions

We have presented a multiphysics simulation study of light- and temperature-programmable ferroelectric domain walls in thin-film lithium niobate, in which the screening-charge relaxation time is set by the sum of a thermally activated dark conductivity and a photo-induced conductivity. The main findings, all of which are model predictions, are as follows. The relaxation law is internally consistent with the simulated time-domain response (agreement within 0.1 ns at moderate illumination), and the predicted behaviour is qualitatively independent of the assumed photoconductivity model. The model predicts an optimum illumination window ($\Phi \approx 0.1$–$1\ \Phi_{sat}$) in which the one-step prediction error of a chaotic time series improves by a factor of 1.7 relative to dark operation, and in which the optimum is task-dependent—illumination tunes the memory–nonlinearity balance. Optical assistance is predicted to enable multilevel nonvolatile programming at low bias, where purely electrical programming writes no resolvable levels. The memory capacity is predicted to remain within 0.95–0.99 over 250–400 K and within 0.98–1.02 for all parameter variations examined, whereas the prediction error varies by less than a factor of 1.6. The system-level energy budget, including illumination and thermal control, is 1.3–9.3 pJ per symbol in the optimum window, and the interferometer bandwidth is predicted to be light-tunable from 27 to 127 MHz. These results provide quantitative design rules and, equally importantly, a set of testable predictions and a measurement protocol for light-programmable domain-wall devices; experimental verification remains the essential next step.

Supplementary Materials: The following supporting information can be downloaded at https://www.mdpi.com/article/10.3390/cryst16100621/s1. Table S1: reference model parameters; Table S2: electro-optic and waveguide parameters; benchmark definitions; reproduction instructions; complete code listings (s7_phototuning.py, s8_figures3.py, s9_photothermal$_{rev}$ision.py, s11_figures$_{fin}$al.py) that generate every figure and table of the manuscript.

Author Contributions: Conceptualization, Y.N.; methodology, Y.N.; software, Y.N.; validation, Y.N. and L.Q.; formal analysis, Y.N.; investigation, Y.N.; resources, L.Q. and C.B.; data curation, C.B.; writing—original draft preparation, Y.N.; writing—review and editing, Y.N., L.Q. and C.B.; visualization, Y.N.; supervision, Y.N.; project administration, Y.N.; funding acquisition, Y.N. All authors have read and agreed to the published version of the manuscript.

Funding: This research was funded by the National Natural Science Foundation of China (Grant No. 12304432) and the Nanxun Scholars Program for Young Scholars of ZJWEU (Grant No. RC2024021394).

Institutional Review Board Statement: Not applicable.

Informed Consent Statement: Not applicable.

Data Availability Statement: The simulation code and data supporting the findings of this study are provided in the Supplementary Materials; raw data arrays are available from the corresponding author upon reasonable request.

Acknowledgments: The authors gratefully acknowledge the financial support of the National Natural Science Foundation of China (Grant No. 12304432) and the Nanxun Scholars Program for Young Scholars of ZJWEU (Grant No. RC2024021394). During the preparation of this manuscript, the authors used an AI language model for language polishing. The authors have reviewed and take full responsibility for the content of this publication.

Conflicts of Interest: The authors declare no conflicts of interest. The funders had no role in the design of the study; in the collection, analyses, or interpretation of data; in the writing of the manuscript; or in the decision to publish the results.

References

1. Wang, C.; Zhang, M.; Chen, X.; Bertrand, M.; Shams-Ansari, A.; Chandrasekhar, S.; Winzer, P.; Lončar, M. Integrated lithium niobate electro-optic modulators operating at CMOS-compatible voltages. *Nature* **2018**, *562*, 101–104. [CrossRef] [PubMed]
2. He, M.; Xu, M.; Ren, Y.; Jian, J.; Ruan, Z.; Xu, Y.; Gao, S.; Sun, S.; Wen, X.; Zhou, L.; et al. High-performance hybrid silicon and lithium niobate Mach–Zehnder modulators for 100 Gbit s^{-1} and beyond. *Nat. Photonics* **2019**, *13*, 359–364. [CrossRef]
3. Zhang, M.; Wang, C.; Kharel, P.; Zhu, D.; Lončar, M. Integrated lithium niobate electro-optic modulators: When performance meets scalability. *Optica* **2021**, *8*, 652–667. [CrossRef]
4. Zheng, Y.; Zhong, H.; Zhang, H.; Song, L.; Liu, J.; Liang, Y.; Liu, Z.; Chen, J.; Zhou, J.; Fang, Z.; et al. Electro-optically programmable photonic circuits enabled by wafer-scale integration on thin-film lithium niobate. *Phys. Rev. Res.* **2023**, *5*, 033206. [CrossRef]
5. Hou, S.; Chen, P.; Shah, M.; Briggs, I.; Xing, W.; Liu, Z.; Fan, L. Programmable optical filter in thin-film lithium niobate with simultaneous tunability of extinction ratio and wavelength. *ACS Photonics* **2023**, *10*, 3896–3900. [CrossRef]
6. Sun, D.; Zhang, Y.; Wang, D.; Song, W.; Liu, X.; Pang, J.; Geng, D.; Sang, Y.; Liu, H. Microstructure and domain engineering of lithium niobate crystal films for integrated photonic applications. *Light Sci. Appl.* **2020**, *9*, 197. [CrossRef] [PubMed]
7. McConville, J.P.V.; Lu, H.; Wang, B.; Tan, Y.; Cochard, C.; Conroy, M.; Moore, K.; Harvey, A.; Bangert, U.; Chen, L.-Q.; et al. Ferroelectric domain wall memristor. *Adv. Funct. Mater.* **2020**, *30*, 2000109. [CrossRef] [PubMed]
8. Chaudhary, P.; Lu, H.; Lipatov, A.; Ahmadi, Z.; McConville, J.P.V.; Sokolov, A.; Shield, J.E.; Sinitskii, A.; Gregg, J.M.; Gruverman, A. Low-voltage domain-wall $LiNbO_3$ memristors. *Nano Lett.* **2020**, *20*, 5873–5878. [CrossRef] [PubMed]
9. Jiang, A.Q.; Geng, W.P.; Lv, P.; Hong, J.-W.; Jiang, J.; Wang, C.; Chai, X.J.; Lian, J.W.; Zhang, Y.; Huang, R.; et al. Ferroelectric domain wall memory with embedded selector realized in $LiNbO_3$ single crystals integrated on Si wafers. *Nat. Mater.* **2020**, *19*, 1188–1194. [CrossRef] [PubMed]
10. Strukov, D.B.; Snider, G.S.; Stewart, D.R.; Williams, R.S. The missing memristor found. *Nature* **2008**, *453*, 80–83, Erratum in *Nature* **2009**, *459*, 1154. [CrossRef] [PubMed]
11. Kim, M.-K.; Lee, J.-S. Ferroelectric analog synaptic transistors. *Nano Lett.* **2019**, *19*, 2044–2050. [CrossRef] [PubMed]
12. Godau, C.; Kämpfe, T.; Thiessen, A.; Eng, L.M.; Haußmann, A. Enhancing the domain wall conductivity in lithium niobate single crystals. *ACS Nano* **2017**, *11*, 4816–4824. [CrossRef] [PubMed]
13. Volk, T.; Wöhlecke, M. *Lithium Niobate: Defects, Photorefraction and Ferroelectric Switching*; Springer Series in Materials Science; Springer: Berlin/Heidelberg, Germany, 2008.

14. Singh, E.; Beccard, H.; Amber, Z.H.; Ratzenberger, J.; Hicks, C.W.; Rüsing, M.; Eng, L.M. Tuning domain wall conductivity in bulk lithium niobate by uniaxial stress. *Phys. Rev. B* **2022**, *106*, 144103. [CrossRef]
15. Werner, C.S.; Herr, S.J.; Buse, K.; Sturman, B.; Soergel, E.; Razzaghi, C.; Breunig, I. Large and accessible conductivity of charged domain walls in lithium niobate. *Sci. Rep.* **2017**, *7*, 9862. [CrossRef] [PubMed]
16. Yakhnevych, U.; Kunzner, M.; Verhoff, L.M.; Ratzenberger, J.; Beyreuther, E.; Rüsing, M.; Sanna, S.; Eng, L.M.; Fritze, H. High-temperature domain wall current in Mg-doped lithium niobate single crystals up to 400 °C. *arXiv* **2024**, arXiv:2404.01214.
17. Ding, L.L.; Beyreuther, E.; Koppitz, B.; Kempf, K.; Ren, J.H.; Chen, W.J.; Rüsing, M.; Zheng, Y.; Eng, L.M. Comparative study of photo-induced electronic transport along ferroelectric domain walls. *Appl. Phys. Lett.* **2024**, *124*, 252901. [CrossRef]
18. Zhang, T.; Garcia Primo, A.; Liu, J.; Gaier, A.; Benea-Chelmus, I.-C. Reconfigurable single-ring photonic molecule on lithium niobate. *arXiv* **2026**, arXiv:2606.06637.
19. Tesfaye, K.S.; Serunjogi, S.M.; Rasras, M.S. High-performance delay-based photonic reservoir computing. *Opt. Express* **2026**, *34*, 24726–24744. [CrossRef] [PubMed]
20. Appeltant, L.; Soriano, M.C.; Van der Sande, G.; Danckaert, J.; Massar, S.; Dambre, J.; Schrauwen, B.; Mirasso, C.R.; Fischer, I. Information processing using a single dynamical node as complex system. *Nat. Commun.* **2011**, *2*, 468. [CrossRef] [PubMed]
21. Buse, K.; Adibi, A.; Psaltis, D. Non-volatile holographic storage in doubly doped lithium niobate crystals. *Nature* **1998**, *393*, 665–668. [CrossRef]
22. Jaeger, H.; Haas, H. Harnessing nonlinearity: Predicting chaotic systems and saving energy in wireless communication. *Science* **2004**, *304*, 78–80. [CrossRef] [PubMed]
23. Atiya, A.F.; Parlos, A.G. New results on recurrent network training: Unifying the algorithms and accelerating convergence. *IEEE Trans. Neural Netw.* **2000**, *11*, 697–709. [CrossRef] [PubMed]
24. Mackey, M.C.; Glass, L. Oscillation and chaos in physiological control systems. *Science* **1977**, *197*, 287–289. [CrossRef] [PubMed]

Disclaimer/Publisher's Note: The statements, opinions and data contained in all publications are solely those of the individual author(s) and contributor(s) and not of MDPI and/or the editor(s). MDPI and/or the editor(s) disclaim responsibility for any injury to people or property resulting from any ideas, methods, instructions or products referred to in the content.